Neural Computing and Applications
https://doi.org/10.1007/s00521-019-04278-7

ORIGINAL ARTICLE

# Fabrication of a portable device for stress monitoring using wearable sensors and soft computing algorithms

Alireza Golgouneh[1] · Bahram Tarvirdizadeh[1]

Received: 5 July 2018 / Accepted: 30 May 2019


**Abstract**
Stress is an issue that everyone experiences in today's modern life. Prolonged exposure to stress can cause many mental and physical diseases. Accordingly, the stress management issue has become popular, and the need for personal healthcare devices has increased in recent years. Therefore, the aim of this research is to design and manufacture a portable stress monitoring system, based on photoplethysmography (PPG) and galvanic skin response (GSR) physiological signals, acquired by wearable sensors. To do so, we proposed a novel algorithm for continuous measurement of the stress index (SI) as well as the classification of stress levels. In order to estimate an accurate value for SI, various soft computing algorithms such as support vector regression, artificial neural networks (ANN), and adaptive neuro-fuzzy inference system (ANFIS) were adopted for modeling the stress based on the features extracted from normalized and non-normalized types of PPG and GSR signals and their combinations. Furthermore, *K*-nearest neighbor (KNN), ANNs, Naive Bayes, and support vector machine (SVM) were utilized to discriminate different levels of stress in subjects. The obtained results indicate that the ANFIS algorithm can estimate the SI training output with the correlation coefficient (CC) of 0.9281 and the average relative error of 0.23 on a subset of the combined features of PPG and GSR signals. Also, the best classification performance was for KNN ($K = 3$) algorithm, with 85.3% accuracy. To evaluate the developed system, data of 16 subjects, out of the training dataset, participated in the experiment in the presence of the experts and psychologists, were used. The average CC of 0.81 and classification accuracy of 75% were obtained, using the implemented ANFIS model and KNN classifier.

**Keywords** Machine learning · Stress · Photoplethysmography · Galvanic skin response · Portable device · Emotion recognition · Physiological signals · Arousal detection

## 1 Introduction

Stress is a familiar experience to all. Excessive stress compromises the immune system by increasing vulnerability to various diseases such as heart disease, brain disorders, and diabetes [1].

The autonomic nervous system (ANS) is divided into the sympathetic nervous system and the parasympathetic nervous system. Both of these systems control the same group of body functions; however, they act in opposite ways. The sympathetic nervous system is responsible for preparing the body for mental and physical activities which is known as the body's "fight-or-flight response" [3]. Contrarily, the parasympathetic nervous system performs almost oppositely and activates the "rest and digest" response [3]. As a result of encountering a stressful factor, the body shows physiological responses including the increase in respiration rate [4] and blood pressure [5], decrease in skin temperature [6], changes in human voice [7–9], heart rate variability (HRV) [10], and pupil diameter (PD) [11] characteristics. In addition to physiological changes, the effects of stress are also manifested in individuals' behavior, which is called "behavioral responses." Changes in face expressions [12, 13], blinking rate [14],

✉ Bahram Tarvirdizadeh
bahram@ut.ac.ir

Alireza Golgouneh
golgouneh@ut.ac.ir

[1] Advanced Service Robots (ASR) Laboratory, Department of Mechatronics Engineering, Faculty of New Sciences and Technologies, University of Tehran, Tehran, Iran

Published online: 07 June 2019

body movements [15], and gazing [14] are some examples of these responses.

Generally, stress can be identified through three different methods including (1) psychological evaluation, (2) behavioral responses (such as analysis of speech, mobile phone usage, computer exposure, facial expressions), and (3) physiological signals [16]. Among physiological signals, electrocardiography (ECG) and HRV [17] are two of the most commonly used in many stress-related studies. In addition, skin temperature [6], electromyography (EMG) [4, 18], blood pressure [19], electroencephalography (EEG) [20, 21], respiration rate [4, 20, 22–24], PD [14, 25], galvanic skin response (GSR) [22, 26–28], and photoplethysmography (PPG) [6, 25, 29] are the other body signs which have been used to detect stress. The simplicity and cost-effectiveness of using PPG and GSR sensors, together with a good correlation of these signals with emotional arousal, have made them popular among the researchers. Empatica [30] and Shimmer [31] are the two data acquisition multi-sensor devices which can capture these signals for real-time applications.

PPG is a technique used to detect the blood-flow changes in blood vessels, noninvasively. In this method, two sensors are used to transmit and receive the infrared light/radiation. The amount of absorbed light by the tissue can lead to changes in the amount of light received by the sensors which consequently create a PPG signal [32]. PPG is a valuable alternative to ECG due to its simplicity in attaching the sensors and providing more physiological information; it has become popular in clinical and non-clinical applications [33].

GSR [which is also known as electrodermal activity (or EDA)], refers to changes in sweat gland activity which is typically measured by applying a small electrical current to the skin surface through two silver-coated (Ag) electrodes. Given the GSR's response to external stimuli, this signal is known as one of the best stress indicators [34].

There are several researches which have extended the topic of classifying the stress into low, medium, and high levels. One of the primary practical studies has been conducted by Healey et al. [22]. In this investigation, the ECG, EMG, respiration, and GSR signals of 24 drivers were collected during the driving process, and their stress levels were classified into three levels. Following this research, the issue of offline or online stress detection has been investigated by the other researches such as [35–38], especially in recent years.

However, given the fact that stress is a continuous feeling, estimating a continuous value for stress in real time is a topic which is yet to be widely explored. One of the other challenges in stress-related works is the lack of comparative study for choosing an appropriate way for signal normalization method. Therefore, in this study, in addition to our primary objective, which is the fabrication of a real-time portable stress monitoring device, we have tried to address these challenges by extracting almost all the extractable features of the PPG and GSR signals and then comparing the various signal normalization methods. In the present study, firstly, the hardware and software of the system are briefly described. Then, we have detailed the modeling (Sect. 3), where we present a method for windowing the signals, followed by window analyses and normalization methods. In order to estimate an accurate value for SI, various techniques such as support vector regression (SVR), artificial neural networks (ANN), and adaptive neuro-fuzzy inference system (ANFIS) have been adopted. Furthermore, *K*-nearest neighbor (KNN), ANNs, Naive Bayes, and support vector machine (SVM) classifiers have been utilized to discriminate the different levels of the stress in subjects and compare the various normalization methods. In Sect. 4, we present the obtained results and discuss their implications. Section 5 concludes and summarizes the present work. Finally, in Sects. 6 and 7, limitations and future works and the appendix of this research are presented.

## 2 Device fabrication

Figure 1 shows the diagram of the fabricated device components, which consist of (1) Sensors, (2) Central Processor and peripheral modules, and (3) Outputs.

### 2.1 Hardware

#### 2.1.1 Sensors

The fabricated stress monitoring device is compatible with both wired fingertip and wireless wristband sensor devices, developed by the Data processing Research Center of RCDAT [39] (Fig. 2). These wearable multi-sensor devices consist of PPG and GSR sensors which sample the analog signals at the 125 Hz frequency. The PPG sensor consists of an infrared light source which transmits 660 nm wavelength light, and a photoelectric cell that converts the transmitted light to electrical signals [40]. Furthermore, sweating increases the skin conductivity which can be measured by applying an electrical current to the skin surface through two silver-coated (Ag) electrodes of the GSR sensor.

#### 2.1.2 Central processor and modules

The BeagleBone Black (BBB) was selected as the central processing board. This small and powerful expansion board is based on AM3358 1 GHz ARM® Cortex-A8 processor

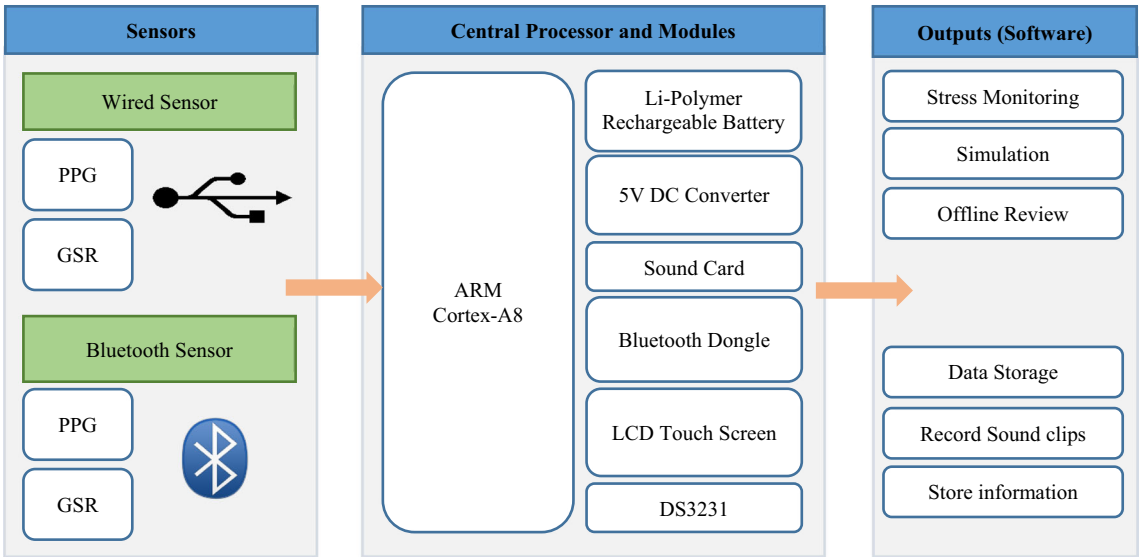


**Fig. 1** Overview of the developed device hardware architecture

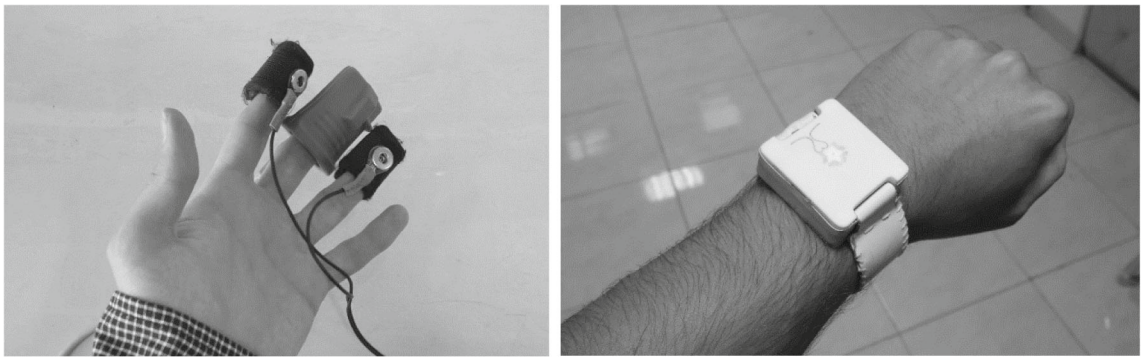

**(a) Wired fingertip sensors** **(b) Wristband wireless sensor**

**Fig. 2** RCDAT biofeedback devices

which has a 512 MB DDR3 RAM and runs the Debian Linux with the 3.8.13-bone kernel operating system. A 3.7 V Li-polymer battery together with MAX756 switching regulator was used to provide a 5 V voltage source for powering the device. To enable the user to interact with the created graphical user interface (GUI), the CS-BBB-EXP43 capacitive touch screen cape was installed on the board. In addition, to keep the accurate time and date information the DS3231 RTC (real-time clock) module was employed which was communicating through the $I^2C$ protocol with the BBB.

## 2.2 Software interface

The device software interface was developed in C++ and QT using the QtCreator IDE in the Intel x64-based processor and Ubuntu 14.04 (64-bit operating system) which was then cross-compiled for ARM v7 Cortex A8 processor. The developed GUI for the system has three functional modes which include real-time, Simulation, and Offline modes (Fig. 22). A sample screenshot of the designed GUI-based application is shown in Fig. 3.

In real-time mode, the signals transmitted from the sensor device are filtered using the online methods, described in [41], for further processing. In this mode, the user's physiological signal and SI can be displayed in real time on the system screen. The other two modes are Offline and Simulation modes, which enable the user to review the information, simulate the recorded data, and edit or remove them.

## 2.3 Case fabrication

The system case was designed in SolidWorks 2013 software with ergonomic and dimensional considerations and then 3D printed using a polylactic acid material with a precision of 240 μm. The actual 3D-printed case is seen in

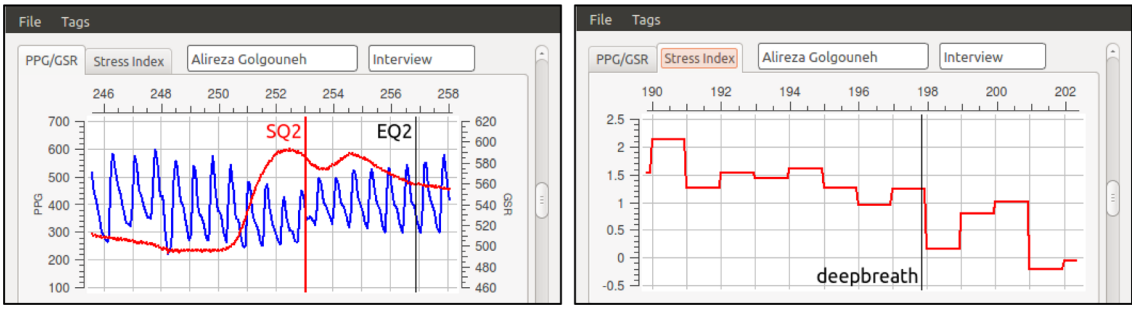


**(a) Displaying the PPG (blue) and GSR (red) signals in real-time mode**

**(b) Real-time displaying of the estimated SI**

**Fig. 3** Sample screenshots of the designed GUI-based application

Fig. 22. Also, screenshots of the model in SolidWorks are seen Fig. 4.

## 3 Modeling

Figure 5 shows the diagram of stress modeling process. In the final step, two models are created to (1) classify the stress levels and (2) estimate the SI.

### 3.1 Dataset

The RCDAT [39] dataset was used in this study. This dataset consists of 63 sessions from 37 volunteers who were compensated for the test. All the tests have been conducted under the controlled conditions and in the presence of experts and psychologists. The audible and visual clips were used to make the Stressful, Normal, and Relaxing phases in volunteers. During the stress phase, a scary movie clip was chosen and played. Similarly, in order to provoke a sense of relaxation in subjects, calming video or sound clips were played under the surveillance of psychologists and experts. It is necessary to mention that at the end of each test, subjects were asked to fill a questionnaire to determine the qualitative level of their stress and relaxation level from 0 to 4. In order to remove the high-frequency noise from PPG signals, a low-pass moving average filter was utilized [41] in the system.

### 3.2 Windowing and labeling

To analyze the bio-signals in real time, signal segmentation method was employed [42–44]. In this method, a window having fixed 20-s length shifts every one second on the signals and the required features are extracted from each segment. As shown in Fig. 6, the two windows have the length of 20 s and the second window has 19-s overlapping with the first window.

In order to label the windows and create the training output, two approaches were utilized. The first technique is discrete labeling which is suitable for the classification. In this method, the windows located entirely within the Stressful, Relaxing, and Normal intervals are labeled with the values of $+1$, $-1$, and 0, respectively. Also, if a window is shared between two states, it will be labeled according to the one which has the most sharing interval.

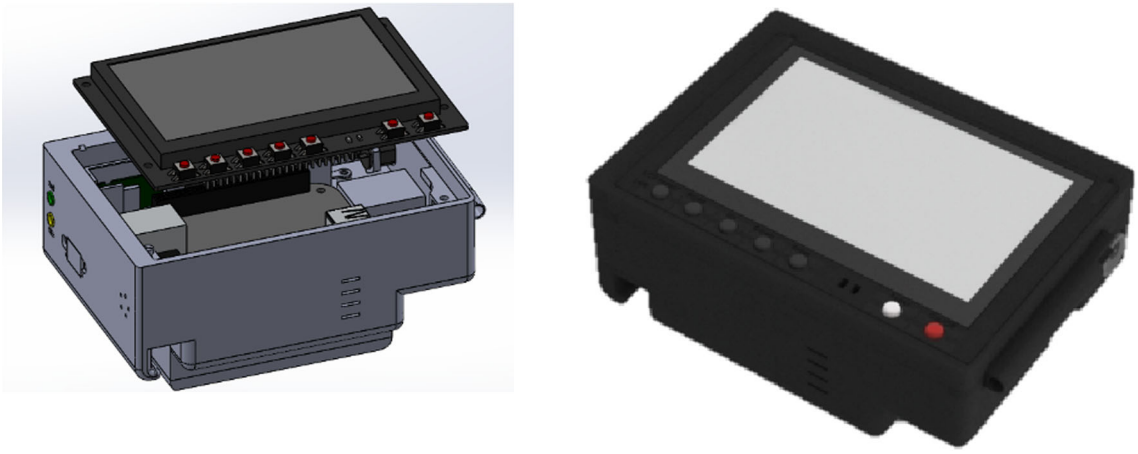

**Fig. 4** 3D CAD model of the Device Case, designed in Solidworks software

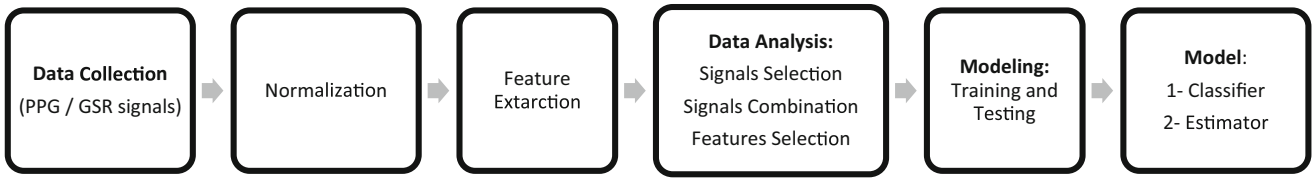


**Fig. 5** Stress Modeling Diagram

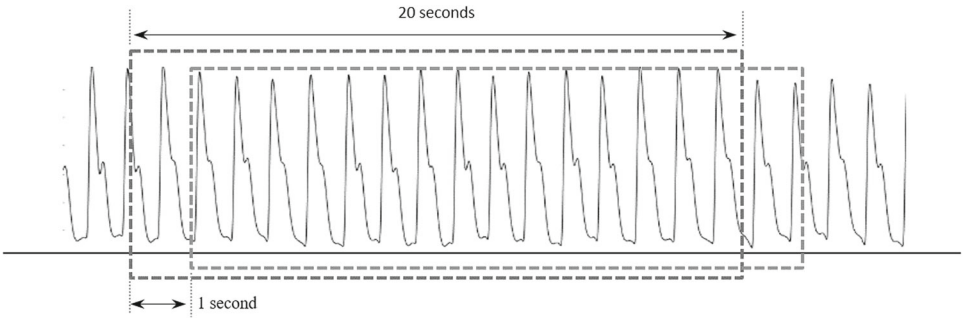


**Fig. 6** Windowing the PPG signal

The second technique is to assign continuous (fuzzy) values to each segment. Similar to the discrete labeling method, windows which are entirely within the Stressful, Relaxing, and Normal periods are + 1, − 1, and 0, respectively. However, if a window ($w$) involves two states, its label (SI($x$)) is calculated through Eq. (1):

$$\mathrm{SI}(x) = \begin{cases} e^{-\frac{(x-c)^2}{2\sigma^2}}, & t_{\text{normal}} < w < t_{\text{stress}} \\ 1 - e^{-\frac{(x-c)^2}{2\sigma^2}}, & t_{\text{stress}} < w < t_{\text{normal}} \\ e^{-\frac{(x-c)^2}{2\sigma^2}} - 1, & t_{\text{relaxing}} < w < t_{\text{normal}} \\ -e^{-\frac{(x-c)^2}{2\sigma^2}}, & t_{\text{normal}} < w < t_{\text{relaxing}} \end{cases} \quad (1)$$

where $C = 0$ and $\sigma = 0.3$ and

$$x_n = -1 + 0.05n, \quad \text{for } i = 1, 2, \ldots, 20 \quad (2)$$

Figure 7 shows an example of the discrete and fuzzy labeling techniques. Window (1) which was entirely located within the normal period was given both a discrete class and fuzzy value of 0; likewise, window (3) received a discrete class and a fuzzy value of + 1 since it was placed within the stress phase. However, since window (2) had the most overlap with stress phase, label + 1 was assigned to this window. In addition, its SI was calculated as $\mathrm{SI}(x_{12}) = 0.4111$ by substituting $x_{12} = -0.4$ into Eq. (1).

### 3.3 Normalization

Normalization of the biological signals is a way to eliminate the interpersonal variations among individuals [22, 25, 45]. In this study, in order to find the appropriate technique of signals normalization for real-time applications, the following three common methods were utilized and compared:

I. Scaling the Signal Amplitude Between − 1 and + 1 [25]

In this method, the signal amplitude is scaled between [− 1 + 1]. In this study, the subscript "mapped" is used to denote a signal normalized by this method.

II. Normalization Using the Baseline [22]

This method is one of the most common normalization techniques which are done by subtracting the baseline and dividing by the signal baseline range:

$$\text{signal}_{\text{normalized}} = \frac{\text{signal} - \min(\text{signal}_{\text{relaxation}})}{\max(\text{signal}_{\text{relaxation}}) - \min(\text{signal}_{\text{relaxation}})} \quad (3)$$

where signal is a raw signal and $\text{signal}_{\text{relaxation}}$ is a baseline signal obtained in the relaxation phase.

III. Standardization [45]

In this method, the signals are centered at zero by subtracting their median and then scaled into 75th–25th percentile (inter-quartile) of their amplitudes. Signals normalized using this method are denoted by the "std" subscript.

### 3.4 Feature extraction

It is worth mentioning that, only, PPG and GSR sensors have been employed in our system. HRV and Cardiotach are not acquired from the different sensors and they are derived from the original PPG signal.

Figure 8 illustrates the diagram of the total features which were extracted from the PPG and GSR signals. According to this figure, 76 features were extracted from

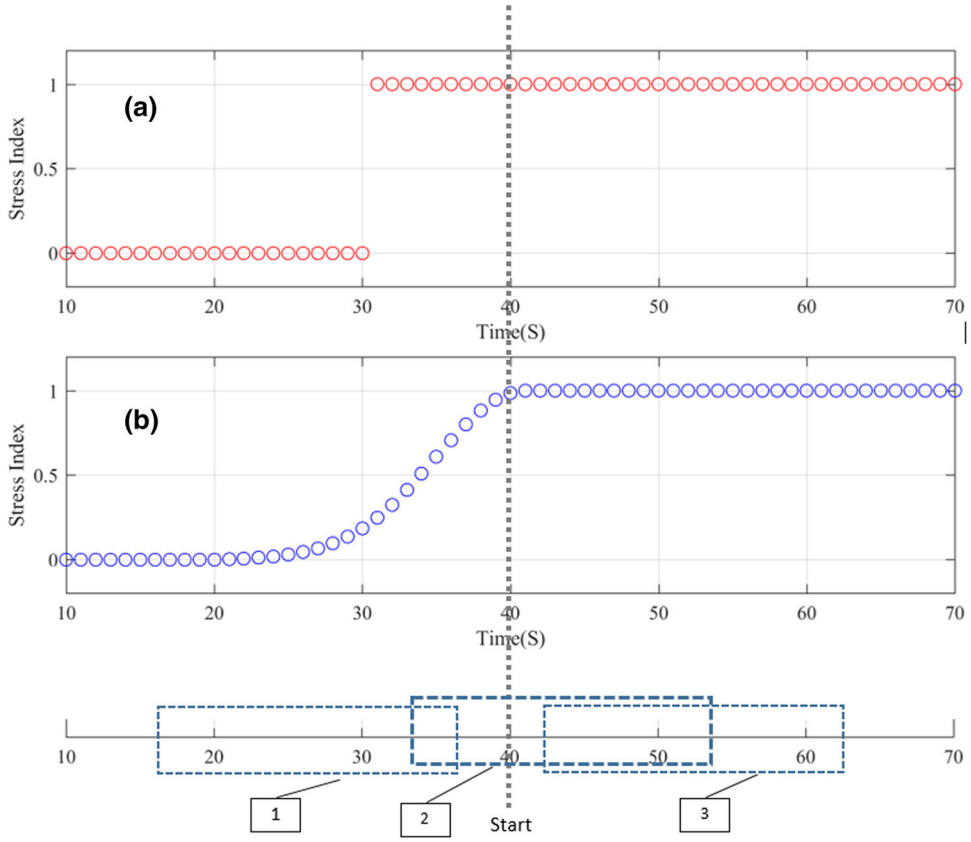


**Fig. 7** An example of **a** discrete and **b** continuous labeling of the time windows

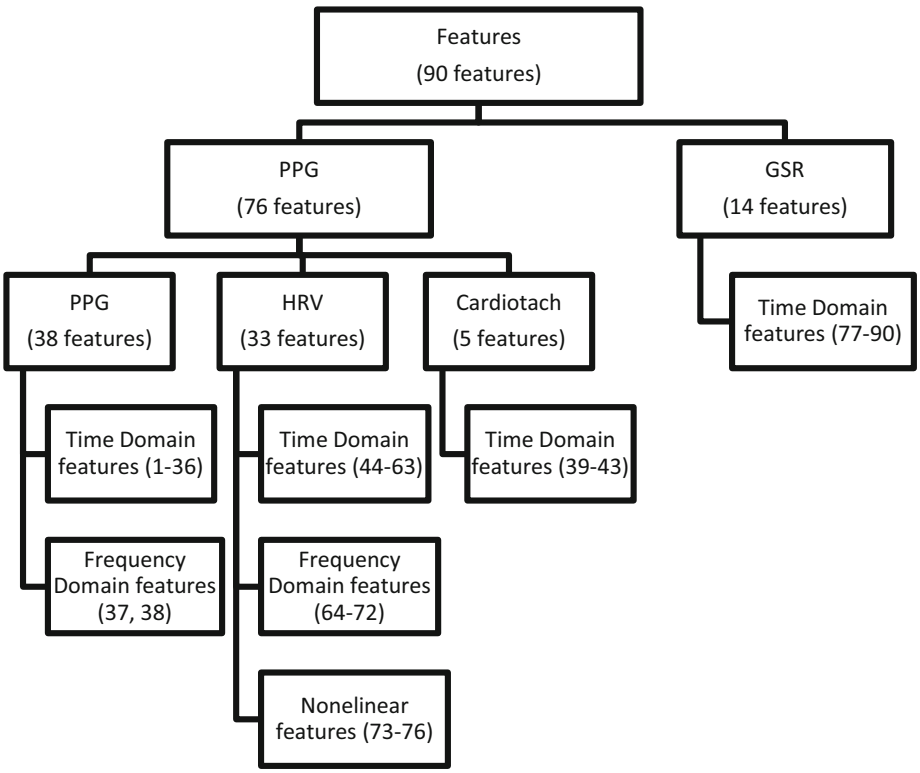


**Fig. 8** The diagram of the extracted features from GSR and PPG and its derivative signals

PPG signal which includes the time and domain frequency features of the actual PPG signal (37 features), HRV (33 features) and Cardiotach features (5).

HRV [46] and Cardiotach [45] are the two signals which are derived from the PPG signal. Figure 9 shows a sample of typical PPG signal and its Cardiotach and HRV signals. In Fig. 9a, the local minima (red points) are called Diastolic Peaks which are the beginnings of heartbeats. The interbeat interval (RRi) is defined as the distance between the two consecutive diastolic peaks which are marked by red dots in the image. The value of RRi is assigned to all points between the two Diastolic peaks which produces a square-wave signal. The square-wave signal is smoothed which finally forms the Cardiotach signal (Fig. 9b). Similar to Cardiotach, HRV signal is defined as 60/RRi which is typically expressed as bpm (beat per minute) (Fig. 9c). In addition to PPG signal features, 14 features were extracted from GSR signals. In order to maintain the coherence of the paper, all the extracted features are described in more details in "Appendix" section and we will only point to their indices here.

## 3.5 Data analysis

### 3.5.1 Signals selection

Before the actual modeling, the similarity of the signals, normalized using the three aforementioned methods, was examined by correlation coefficient of their feature vectors.

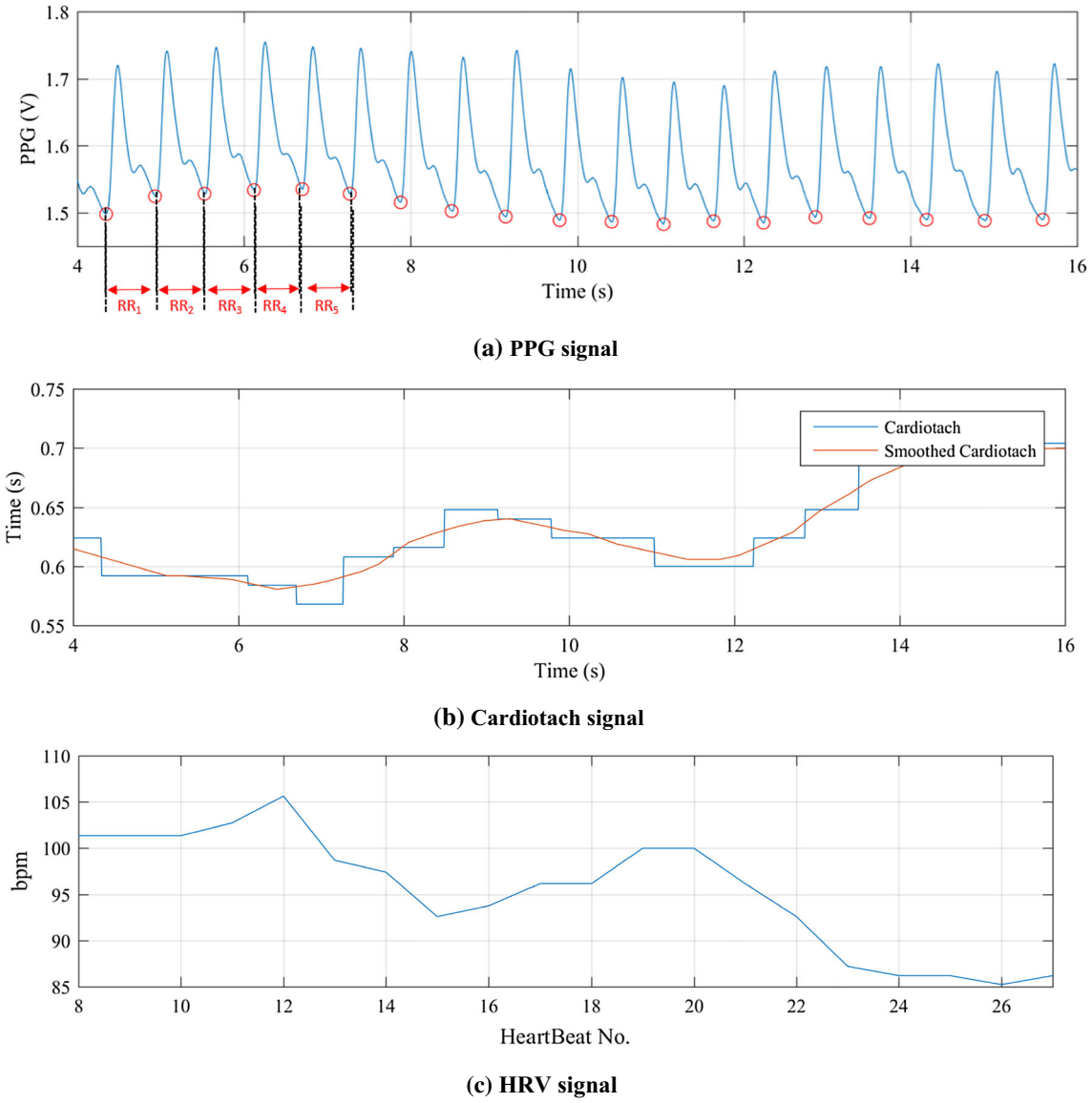


**Fig. 9** A sample **a** PPG signal, and its derivative **b** Cardiotach and **c** HRV signals

**Table 1** Correlation analysis between feature vectors of the GSR signals normalized by different methods

| Signal | GSR | $GSR_{mapped}$ | $GSR_{normalized}$ | $GSR_{std}$ |
|---|---|---|---|---|
| GSR | 1 | 0.99298 | 0.737614 | 0.769869 |
| $GSR_{mapped}$ | 0.99298 | 1 | 0.734194 | 0.77027 |
| $GSR_{normalized}$ | 0.737614 | 0.734194 | 1 | 0.75177 |
| $GSR_{std}$ | 0.769869 | 0.77027 | 0.75177 | 1 |

**Table 2** Correlation analysis between PPG and $PPG_{std}$

| Signal | PPG | $PPG_{std}$ |
|---|---|---|
| PPG | 1 | 0.9608 |
| $PPG_{std}$ | 0.9608 | 1 |

Based on the results reported in Tables 1 and 2, it is evident that the feature vectors of the GSR signal (without normalization) and $GSR_{mapped}$ were highly correlated having the CC of 0.99, leading to the same modeling results. Therefore, the $GSR_{mapped}$ was removed from the stress modeling process. Similarly, $PPG_{std}$ feature vectors had the CC of 0.96 with the PPG feature sets and it was eliminated from the training set too.

#### 3.5.2 Signals combination

In order to compare the results and find the appropriate subset of the features, which leads to the highest classification and estimation accuracy, at first, each signal including PPG, GSR, $GSR_{std}$, and $GSR_{normalized}$ signals and then the different combinations of them including PPG + GSR, PPG + $GSR_{normalized}$, and PPG + $GSR_{std}$ were analyzed.

#### 3.5.3 Features selection

Since some of the features were correlated or dependent on each other, they could negatively impact the modeling result. In addition, selection of fewer features leads to minimizing the modeling and detection time. Therefore, the four filter feature selection methods, namely MRMR [47], OSFS [48], Chi-square [49], and Alpha-investing [50], were adopted to find the irrelevant features from the dataset. These filter-based methods filter out redundant features independently from the classification algorithms [51]. The results of applying these algorithms on the extracted features are mentioned in Table 3. In this table, "Feature indices" refer to the feature indices listed in "Appendix" section.

### 3.6 Classification

*K*-nearest neighbor (KNN), Naive Bayes, support vector machine (SVM) with Gaussian kernel, radial basis function (RBF) [52] and multi-layer perceptron (MLP) [53] artificial neural networks (ANNs) were used to detect three different levels of stress situations including high stress or "Stressful," moderate stress or "Normal" and baseline or "Relaxing." After several experiments, the desired configurations for the MLP and the RBF ANNs were obtained and are reported in Tables 4 and 5, respectively.

### 3.7 Estimating the SI

Support vector regression (SVR), MLP and RBF ANNs and adaptive neuro-fuzzy inference system (ANFIS) [54] with the parameters mentioned in Table 6 were utilized to model and estimate the SI. Through the implementation of the overlapping windowing method described in Sect. 3.2, 6101 windows were extracted and labeled. Figure 10 shows a segmentation of the modeling training output obtained using the continuous labeling approach, detailed in Sect. 3.2. It should be mentioned that the windows with + 1, − 1, and 0 values outnumbered the fuzzy labeled windows. Such imbalances often lead to inaccurate results by biasing the estimations toward the overlearned classes and labels. To address this problem, 3173 windows were selected randomly so that the number of the windows with the values of + 1, − 1, and 0 were approximately equal to the fuzzy ones.

## 4 Results and discussion

In this section, we have discussed and detailed the feature selection, classification, SI estimation, and device evaluation results:

### 4.1 Feature selection results

As mentioned in Sect. 3, 14 time and frequency domain features were extracted from the GSR signal. In addition, 38 features from PPG, 33 features from the derived HRV, and five features from the derived Cardiotach signals were extracted as outlined in Appendix section. To identify the most significant features, MRMR, OSFS, Chi-square, and Alpha-investing feature selection algorithms were applied to the extracted features. Information provided in Table 3 reveals that among the GSR features, the features with #83 and #84 indices, namely "The amplitude of the highest Skin Conductance Responses (SCRs)" and "The rise time of the highest SCR," were selected by almost all the

**Table 3** The result of applying feature selection methods on the extracted features

| Bio-signal | Feature selection methods | | | | | | | |
|---|---|---|---|---|---|---|---|---|
| | Alpha-investing | | OSFS | | MRMR | | Chi-square | |
| | No. of features | Feature indices | No. of features | Feature indices | No. of features | Feature indices | No. of features | Feature indices |
| GSR | 10 | 77, 78, 79, 80, 81, 82, 83, 84, 87, 88 | 2 | 83, 84 | 13 | 77, 78, 79, 80, 81, 82, 83, 84, 85, 86, 87, 88, 89 | 14 | 77, 78, 79, 80, 81, 82, 83, 84, 85, 86, 87, 88, 89, 90 |
| $GSR_{normalized}$ | 5 | 77, 79, 82, 83, 84 | 2 | 83, 84 | 1 | 83 | 14 | 77, 78, 79, 80, 81, 82, 83, 84, 85, 86, 87, 88, 89, 90 |
| $GSR_{std}$ | 8 | 77, 78, 79, 80, 81 82, 83, 84 | 2 | 83, 84 | 1 | 83 | 14 | 77, 78, 79, 80, 81, 82, 83, 84, 85, 86, 87, 88, 89, 90 |
| PPG | 3 | 44, 45, 69 | 2 | 44, 69 | 1 | 69 | 21 | 39, 40, 41, 42, 43, 44, 45, 47, 50, 51, 54, 56, 62, 63, 66, 68, 69, 72, 74, 75, 76 |
| PPG + GSR | 4 | 54, 69, 83, 84 | 2 | 69, 84 | 1 | 69 | 30 | 39, 40, 41, 42, 43, 44, 45, 47, 50, 51, 54, 56, 62, 63, 66, 68, 69, 72, 74, 75, 76, 77, 78, 79, 80, 81 82, 83, 84, 89 |
| PPG + $GSR_{normalized}$ | 3 | 54, 69, 84 | 2 | 69, 84 | 1 | 69 | 30 | 39, 40, 41, 42, 43, 44, 45, 47, 50, 51, 54, 56, 62, 63, 66, 68, 69, 72, 74, 75, 76, 77, 78, 79, 80, 81 82, 83, 84, 89 |
| PPG + $GSR_{std}$ | 10 | 44, 45, 54, 56, 69, 76, 77, 82, 83, 84 | 2 | 69, 84 | 1 | 69 | 30 | 39, 40, 41, 42, 43, 44, 45, 47, 50, 51, 54, 56, 62, 63, 66, 68, 69, 72, 74, 75, 76, 77, 78, 79, 80, 81 82, 83, 84, 89 |

**Table 4** Parameters of the MLP neural network model

| No. | Factor/method | Magnitude/explanation |
|---|---|---|
| 1 | Hidden layers number | 1 |
| 2 | Training method | Levenberg–Marquardt |
| 3 | Hidden neurons activation function | tan*h* (Sigmoid) |
| 4 | Output neurons activation function | Linear mapping |
| 5 | Loss function | RMSE (Root-mean-square error) |
| 6 | Extreme number of training epochs | 20 |
| 7 | The least error of training | $10^{-5}$ |
| 8 | Pre-conditioning of the input data | 1. Removing constant input<br>2. Input data normalizing to the [0, 1] range |

selection methods. These features were previously introduced and used in [55]. In addition, the features with indices of #44 and #69, namely the "Average Heart Rate" and "LF/HF ratio," were selected by the most effective PPG features. These features have been used in the previous studies including [56]. Furthermore, none of the features #1 to #37 (known as PPG waveform characteristics introduced in [57–59]) were selected by the feature selectors, and it can be claimed that they had the least correlation with stress labels.

## 4.2 Classification results

Prior to reporting the classification results, it should be mentioned that for comparing the classifiers, prediction accuracy has been used which can be expressed as the percentage of the correctly classified windows over the total number of windows. In addition, a tenfold cross-validation technique has been used to evaluate the models.

**Table 5** Parameters of the rbf neural network model

| No. | Factor/method | Magnitude/explanation |
|---|---|---|
| 1 | Training method | Least-square |
| 2 | Estimation algorithm of the number of the hidden neurons | Subtractive clustering |
| 3 | Hidden neurons activation function | Radial basis function (Gaussian) |
| 4 | Output neurons activation function | Weighted summation |
| 5 | Loss function | RMSE (Root-mean-square error) |
| 6 | Extreme number of training epochs | 20 |
| 7 | The least error of training | $10^{-5}$ |
| 8 | Pre-conditioning of the input data | 1. Removing constant input |
| | | 2. Input data normalizing to the [0, 1] range |

**Table 6** Parameters of the ANFIS model

| No. | Factor/method | Magnitude/explanation |
|---|---|---|
| 1 | Training method | Back-propagation |
| 2 | Clustering technique | Grid-partitioning, subtractive, and C-means |
| 3 | Membership function of the input | Gaussian (gaussmf) |
| 4 | Membership function of the output | Linear mapping |
| 5 | Loss function | RMSE (Root-mean-square error) |
| 6 | Extreme number of training epochs | 20 |
| 7 | The least error of training | $10^{-5}$ |
| 8 | Pre-conditioning of the input data | 1. Removing constant input |
| | | 2. Input data normalizing to the [0, 1] range |

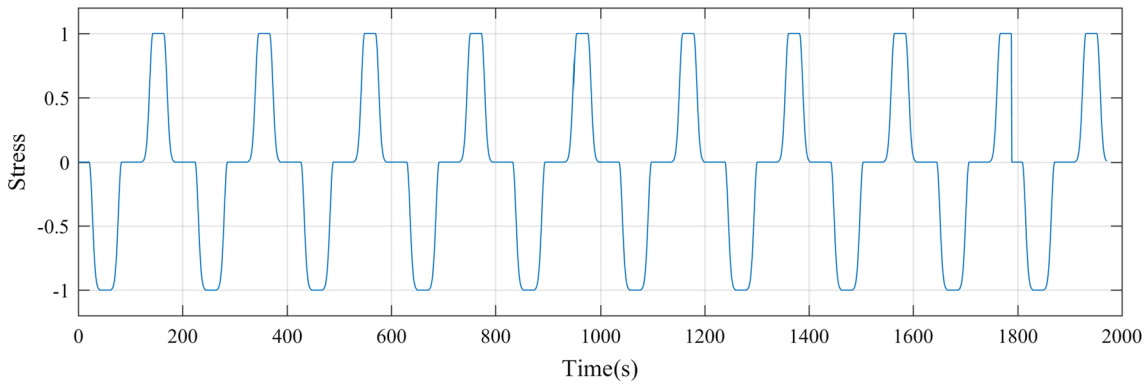


**Fig. 10** Continuous stress objective function

In the following classification plots, the horizontal axis denotes the PPG and GSR signals and their combinations, and the vertical axis indicates the average classification accuracy using the tenfold cross-validation on the subset of features which are selected by the aforementioned four feature selection algorithms.

Figures 11, 12 and 13 together with Tables 7, 8 and 9 show the results of the KNN classifier with $K = 3, 5, 7$, respectively. It is evident that the best performances among these classifiers belong to the 3-NN classifier run on the PPG + GSR and PPG + $GSR_{std}$ feature sets with the accuracies of 85% and 83.89%, respectively. Figure 14 and Table 10 show that the MLP ANN on the subset of PPG + $GSR_{normalized}$ features (77.4% accuracy) selected by Chi-square method was slightly better than the RBF ANN on PPG + GSR features (74.03% accuracy) (Fig. 15 and Table 11). In addition, Fig. 17 and Table 13 show the results of the SVM classification. Compared to the other

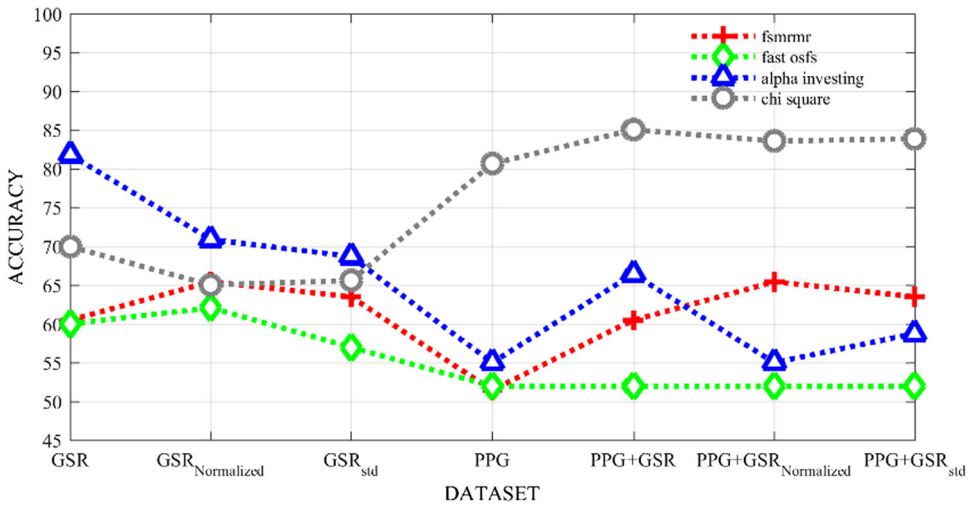


**Fig. 11** The prediction accuracy by KNN ($K = 3$) classifier

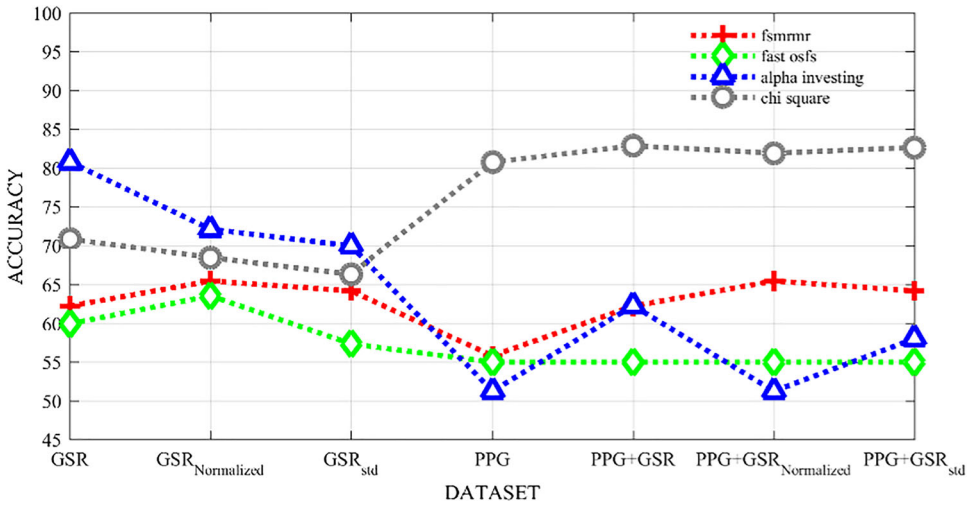


**Fig. 12** The prediction accuracy by KNN ($K = 5$) classifier

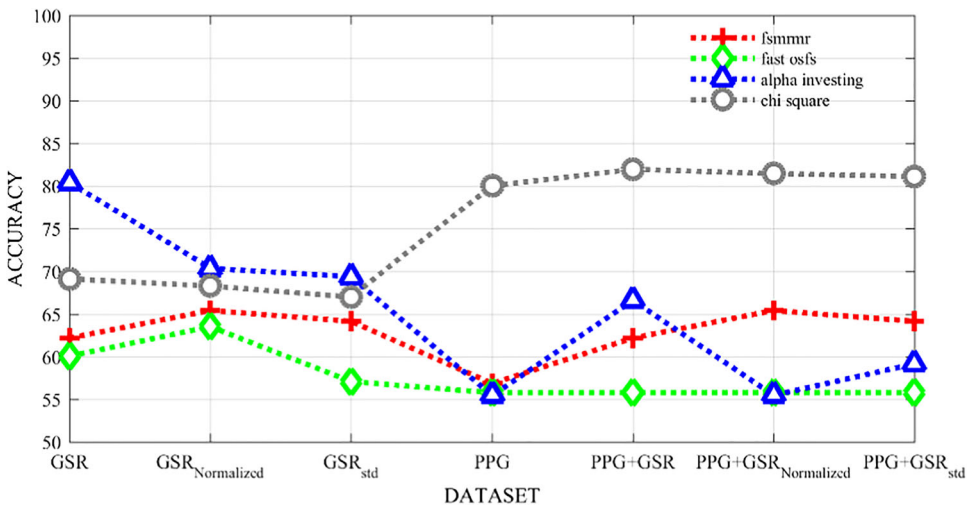


**Fig. 13** The prediction accuracy by KNN ($K = 7$) classifier

features selection methods, features selected by the Chi-square method led to the better performance with 76.14% accuracy in this classification. Naive Bayes with 70.96% accuracy had a relatively lower performance compared to the other classifiers (Fig. 16 and Table 12).

**Table 7** The prediction accuracy by KNN ($K = 3$) classifier

| Feature selection methods | | | | Bio-signal |
|---|---|---|---|---|
| Alpha-investing | OSFS | MRMR | Chi-square | |
| 81.81 | 60.01 | 60.5 | 70 | GSR |
| 70.87 | 62.1 | 65.45 | 65.05 | $GSR_{normalized}$ |
| 68.69 | 56.99 | 63.52 | 65.61 | $GSR_{std}$ |
| 55.01 | 51.97 | 51.45 | 80.65 | PPG |
| 66.41 | 51.97 | 60.5 | *85.03* | PPG + GSR |
| 55.01 | 51.97 | 65.45 | 83.58 | PPG + $GSR_{normalized}$ |
| 58.77 | 51.97 | 63.52 | 83.89 | PPG + $GSR_{std}$ |

The best obtained result is written in italics

**Table 8** The prediction accuracy by KNN ($K = 5$) classifier

| Feature selection methods | | | | Bio-signal |
|---|---|---|---|---|
| Alpha-investing | OSFS | MRMR | Chi-square | |
| 80.76 | 59.92 | 62.21 | 70.81 | GSR |
| 72.09 | 63.45 | 65.45 | 68.45 | $GSR_{normalized}$ |
| 69.94 | 57.34 | 64.18 | 66.32 | $GSR_{std}$ |
| 51.23 | 54.97 | 55.79 | 80.74 | PPG |
| 62.27 | 54.97 | 62.21 | *82.85* | PPG + GSR |
| 51.23 | 54.97 | 65.45 | 81.91 | PPG + $GSR_{normalized}$ |
| 57.99 | 54.97 | 64.18 | 82.63 | PPG + $GSR_{std}$ |

The best obtained result is written in italics

**Table 9** The prediction accuracy by KNN ($K = 7$) classifier

| Feature selection methods | | | | Bio-signal |
|---|---|---|---|---|
| Alpha-investing | OSFS | MRMR | Chi-square | |
| 80.4 | 60.08 | 62.21 | 69.14 | GSR |
| 70.36 | 63.56 | 65.45 | 68.32 | $GSR_{normalized}$ |
| 69.39 | 57.1 | 64.18 | 67.03 | $GSR_{std}$ |
| 55.48 | 55.79 | 56.88 | 80.01 | PPG |
| 66.63 | 55.79 | 62.21 | *81.96* | PPG + GSR |
| 55.48 | 55.79 | 65.45 | 81.45 | PPG + $GSR_{normalized}$ |
| 59.17 | 55.79 | 64.18 | 81.12 | PPG + $GSR_{std}$ |

The best obtained result is written in italics

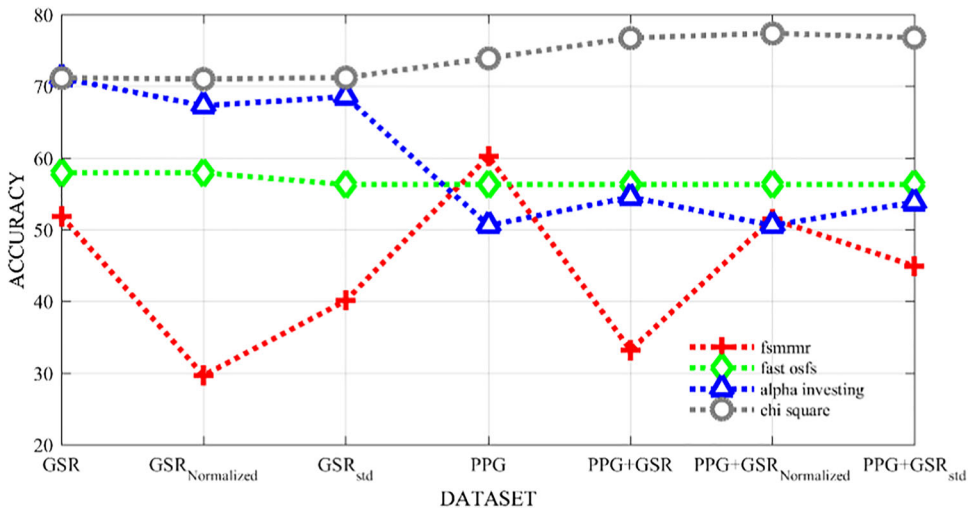


**Fig. 14** The prediction accuracy by MLP ANN classifier

**Table 10** The prediction accuracy by MLP ANN classifier

| Feature selection methods | | | | Bio-signal |
|---|---|---|---|---|
| Alpha-investing | OSFS | MRMR | Chi-square | |
| 71.14 | 57.92 | 51.86 | 71.18 | GSR |
| 67.28 | 57.92 | 29.66 | 71.01 | $GSR_{normalized}$ |
| 68.54 | 56.3 | 40.1 | 71.21 | $GSR_{std}$ |
| 50.59 | 56.3 | 60.21 | 73.92 | PPG |
| 54.54 | 56.3 | 33.21 | 76.74 | PPG + GSR |
| 50.59 | 56.3 | 51.48 | *77.4* | PPG + $GSR_{normalized}$ |
| 53.88 | 56.3 | 44.92 | 76.78 | PPG + $GSR_{std}$ |

The best obtained result is written in italics

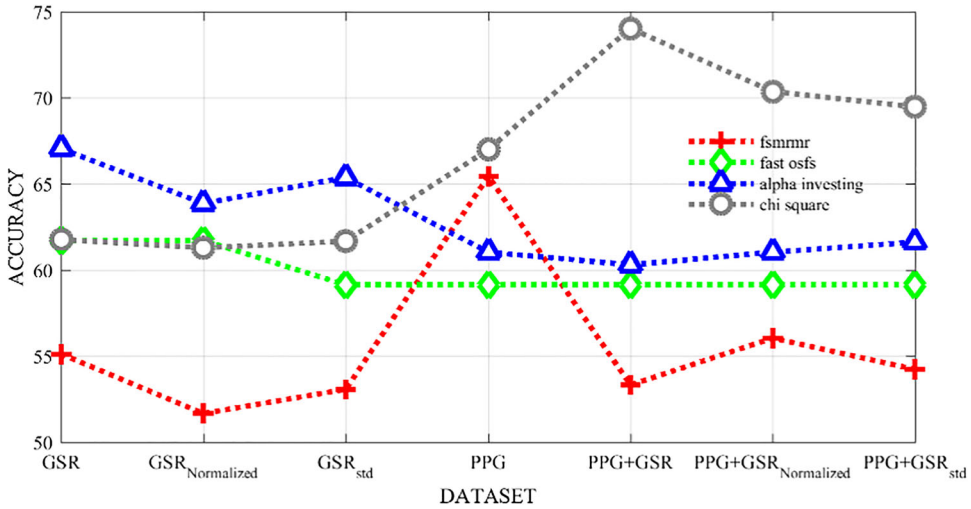


**Fig. 15** The prediction accuracy by RBF ANN classifier

**Table 11** The prediction accuracy by RBF ANN classifier

| Feature selection methods | | | | Bio-signal |
|---|---|---|---|---|
| Alpha-investing | OSFS | MRMR | Chi-square | |
| 67.05 | 61.7 | 55.12 | 61.76 | GSR |
| 63.87 | 61.7 | 51.66 | 61.28 | $GSR_{normalized}$ |
| 65.38 | 59.16 | 53.06 | 61.67 | $GSR_{std}$ |
| 61.03 | 59.16 | 65.45 | 66.99 | PPG |
| 60.3 | 59.16 | 53.32 | *74.03* | PPG + GSR |
| 61.03 | 59.16 | 56.05 | 70.36 | PPG + $GSR_{normalized}$ |
| 61.61 | 59.16 | 54.23 | 69.47 | PPG + $GSR_{std}$ |

The best obtained result is written in italics

### 4.3 Estimation results

As noted earlier, one of the objectives of this study was to find a reliable way to estimate the actual value for an individual's stress level which was done by the proposed method for determining a training output, as described in the Sect. 3.2. Figures 18, 19, 20, and 21 show the performance of the models used to estimate the SI. In addition, the estimation results are summarized in Table 14. Regarding the classification results, since the best results for the MLP ANN method were obtained with the features selected by the Chi-square method from PPG + $GSR_{normalized}$ signals (Table 10), the same features were also used to create the estimator model (shown in Fig. 18). At best, the CC reached 0.86, when the 40 neurons were chosen for the hidden layer. Furthermore, employing the RBF ANN classification features led to the 0.74 CC (Fig. 19). The CC value for ANFIS was relatively higher than that for the

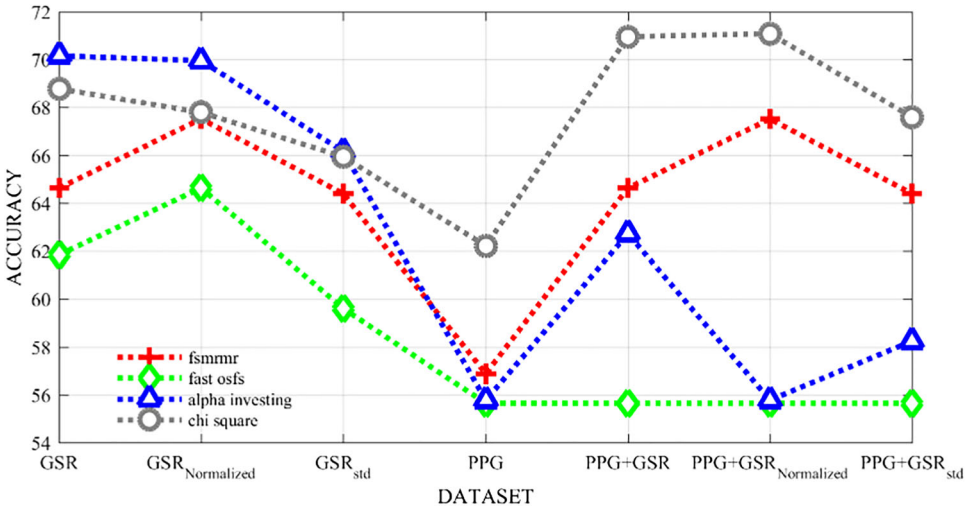


**Fig. 16** The prediction accuracy by Naive Bayes classifier

**Table 12** The prediction accuracy by Naive Bayes classifier

| Feature selection methods | | | | Bio-signal |
|---|---|---|---|---|
| Alpha-investing | OSFS | MRMR | Chi-square | |
| 70.16 | 61.85 | 64.63 | 68.78 | GSR |
| 69.96 | 64.63 | 67.52 | 67.79 | $GSR_{normalized}$ |
| 66.16 | 59.61 | 64.39 | 65.94 | $GSR_{std}$ |
| 55.77 | 55.65 | 56.88 | 62.21 | PPG |
| 62.72 | 55.65 | 64.63 | *70.96* | PPG + GSR |
| 55.77 | 55.65 | 67.52 | 70.19 | PPG + $GSR_{normalized}$ |
| 58.26 | 55.65 | 64.39 | 67.59 | PPG + $GSR_{std}$ |

The best obtained result is written in italics

**Table 13** The prediction accuracy by SVM classifier

| Feature selection methods | | | | Bio-signal |
|---|---|---|---|---|
| Alpha-investing | OSFS | MRMR | Chi-square | |
| 73.2 | 58.61 | 55.97 | 65.87 | GSR |
| 66.12 | 62.85 | 65.74 | 67.41 | $GSR_{normalized}$ |
| 65.68 | 54.43 | 64.39 | 65.23 | $GSR_{std}$ |
| 55.12 | 51.41 | 56.88 | 60.54 | PPG |
| 62.14 | 51.41 | 55.97 | *76.14* | PPG + GSR |
| 55.12 | 51.41 | 65.74 | 71.47 | PPG + $GSR_{normalized}$ |
| 57.41 | 51.41 | 64.39 | 70.9 | PPG + $GSR_{std}$ |

The best obtained result is written in italics

other methods. By remodeling with various subsets of data and different clustering methods including Grid-Partitioning, Subtractive, and C-Means, the best result was finally obtained with the use of subtractive clustering (with the cluster radius of 0.5) on the features selected by the Chi-square algorithm from a combination of PPG and GSR (Fig. 20). The resulting accuracy of 0.92 was the highest accuracy among the modeling methods. Obtained results also show that the SVR algorithm is able to follow the training stress output with a CC of 0.88 (Fig. 21).

## 4.4 Evaluation of the system

For evaluating the developed system, 16 healthy people out of the training set with an average age and standard deviation of 25 ± 1.2 participated in the experiment in the presence of experts and psychologists. To make the

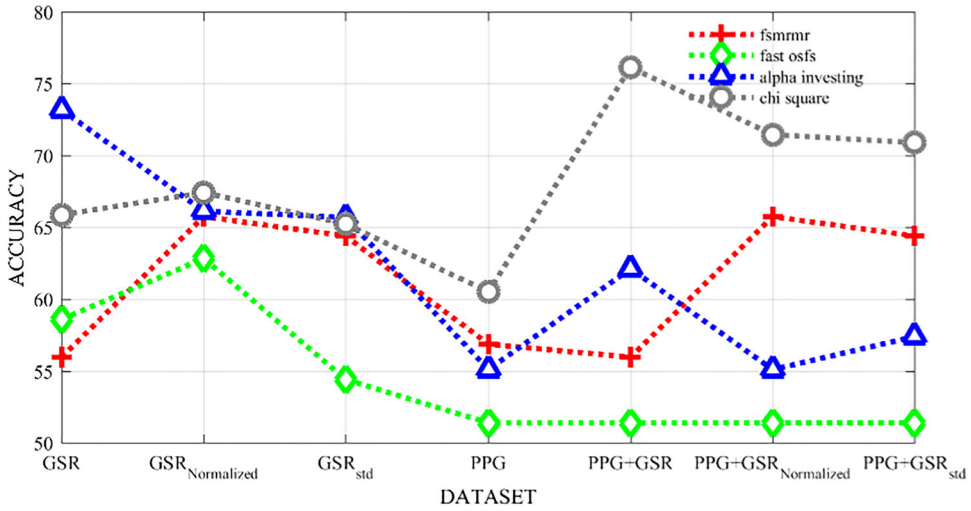


**Fig. 17** The prediction accuracy by SVM classifier

"Stressful" and "Relaxing" situations, audible and visual movie clips were utilized and after each test volunteers were asked to fill out a questionnaire to verify the level of their stress and calmness during the tests. The data were sampled at a 125 Hz rate from fingertip sensors. From the 953 extracted windows, 724 of them were correctly classified with the accuracy of 75%. Also, the estimated SI had an average CC of 0.81 with the expected output, using the implemented ANFIS model.

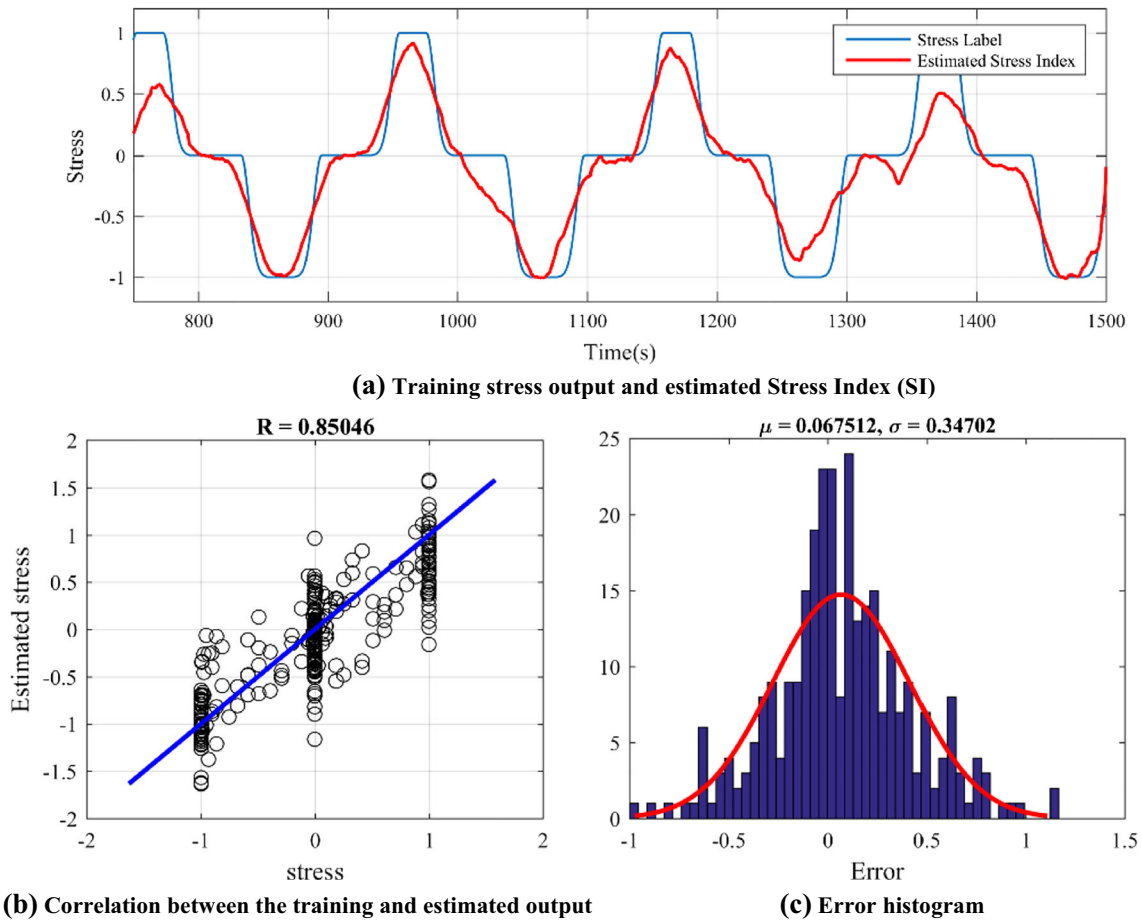


**(a) Training stress output and estimated Stress Index (SI)**

**(b) Correlation between the training and estimated output**

**(c) Error histogram**

**Fig. 18** Results of the estimation using MLP ANN

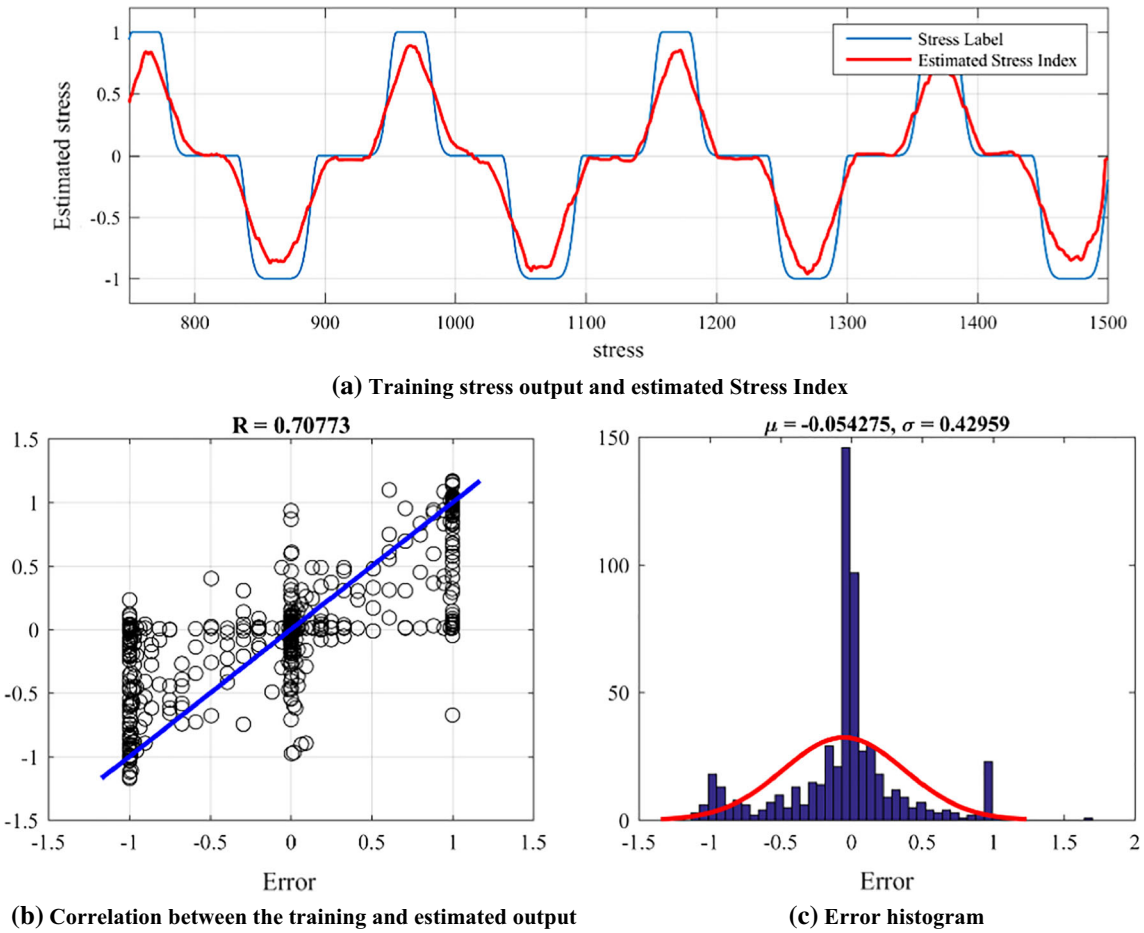


**(a) Training stress output and estimated Stress Index**

**(b) Correlation between the training and estimated output**

**(c) Error histogram**

**Fig. 19** Results of the estimation using RBF ANN

## 5 Conclusion

Stress is an issue that every person experiences every day. Although stress is necessary for survival, excessive stress can be detrimental and may cause harmful diseases including cardiovascular disorders, diabetes, and so on. Therefore, designing and manufacturing a portable stress analyzing and monitoring system was the main subject of this research.

To this end, PPG and GSR signals were obtained from the volunteers who were stressed and then relaxed. By applying the 20-s signal segmentation method, 90 features were extracted from each analyzing window. For determining the training label of each segmentation, a novel method was proposed. Then, to compare the commonly used normalization methods, the signals and extracted features were normalized.

The results showed that the feature vectors of the GSR signals normalized by scaling the signal amplitude between $[-1 +1]$ interval had a CC of 0.99 with the features of non-normalized GSR signals. Likewise, the feature vectors of the standardized PPG signals had almost 0.96 CC with the non-standardized PPG signals. Therefore, these signals were eliminated from the signal sets. Having applied four feature selection algorithms including MRMR, OSFS, Chi-square, and Alpha-investing, the features that had fewer effects on the stress labels were discarded. In order to estimate an accurate value for SI, various techniques such as support vector regression (SVR), artificial neural networks (ANN), and adaptive neuro-fuzzy inference system (ANFIS) were adopted. Furthermore, *K*-nearest neighbor (KNN), ANNs, Naive Bayes, and support vector machine (SVM) classifiers were used to discriminate the different levels of the stress in subjects.

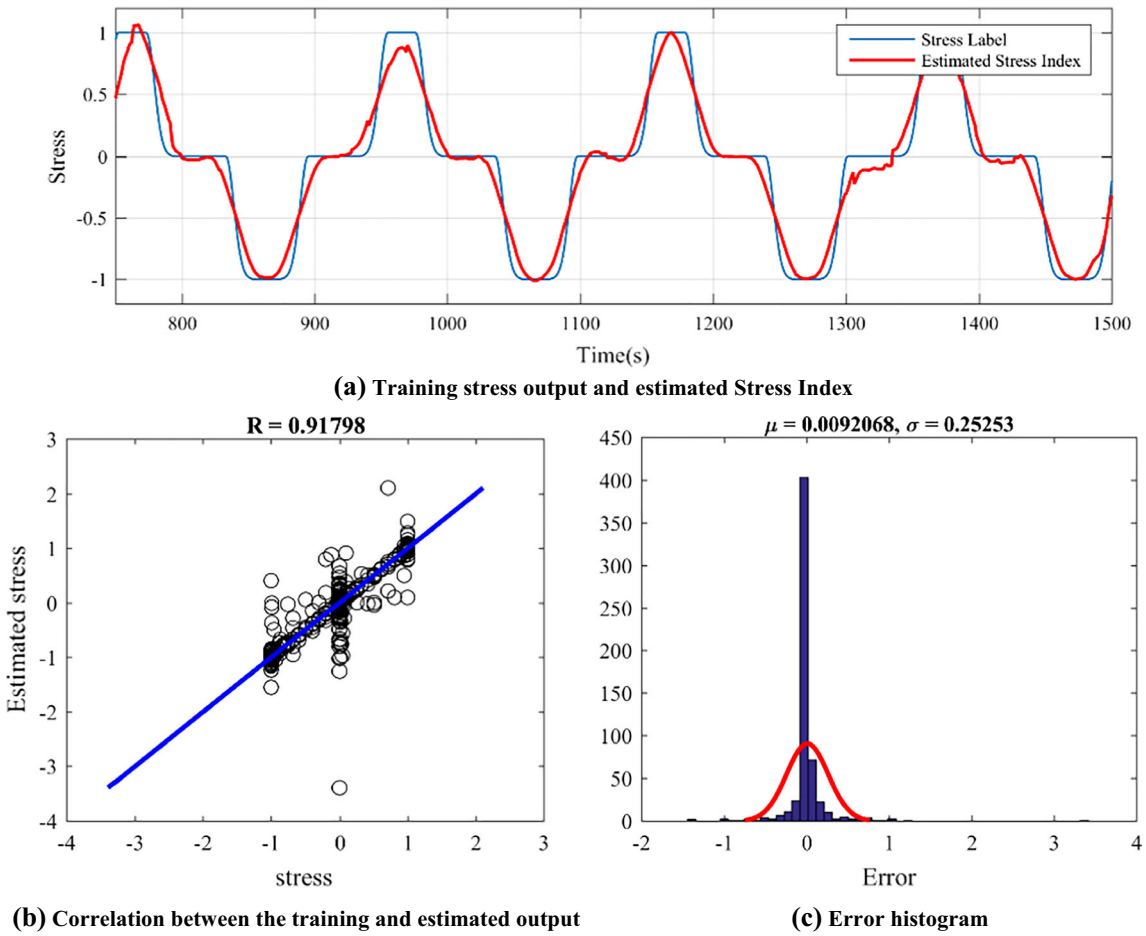


**(a)** Training stress output and estimated Stress Index

**(b)** Correlation between the training and estimated output

**(c)** Error histogram

**Fig. 20** Results of the estimation using ANFIS

As stated in Sect. 4, the best performances for classifying stress into three stress levels (including high stress or "Stressful," moderate stress or "Normal" and baseline or "Relaxing") were achieved with the 3-NN classifier run on the PPG + GSR and PPG + $GSR_{std}$ feature sets with the accuracy of 85% and 83.89%, respectively. The third best in terms of the accuracy was for the SVM classification at 76.14% accuracy on the PPG + GSR features (Fig. 17 and Table 13). Figure 14 and Table 10 show that the MLP ANN on the subset of PPG + $GSR_{normalized}$ features selected by the Chi-square method, with the accuracy of 77.4%, was slightly better than applying the RBF ANN on PPG + GSR features at 74.03% accuracy.

A summary of the SI estimation results is mentioned in Table 14. As depicted in Fig. 20, the best SI estimation result was obtained by the use of subtractive clustering (with the cluster radius of 0.5) and the features selected by the Chi-square algorithm from a combination of the PPG and GSR signals. Accordingly, MLP, RBF, and SVR had CCs of 0.86, 0.74 and 0.88, respectively. The details of these networks configurations and their parameters can be found in Sect. 3.

Finally, the models with the best performance were chosen and implemented on the fabricated device. To evaluate the developed system, 16 subjects out of the training dataset used to evaluation. The average CC of 0.81 and the classification accuracy of 75% were obtained using the implemented ANFIS model and KNN classifier.

The developed system, depicted in Fig. 22, is able to detect and monitor the individual's stress in real time. The device is based on ARM-processor and it can be connected to wired and/or wireless wearable sensors. The GUI of the system is created using C++ and QT, and the system has three functional modes. The real-time mode was developed to monitor the user's physiological signal and SI in real time. In addition, the Offline and Simulation modes enable the user to review the information and simulate the recorded data.

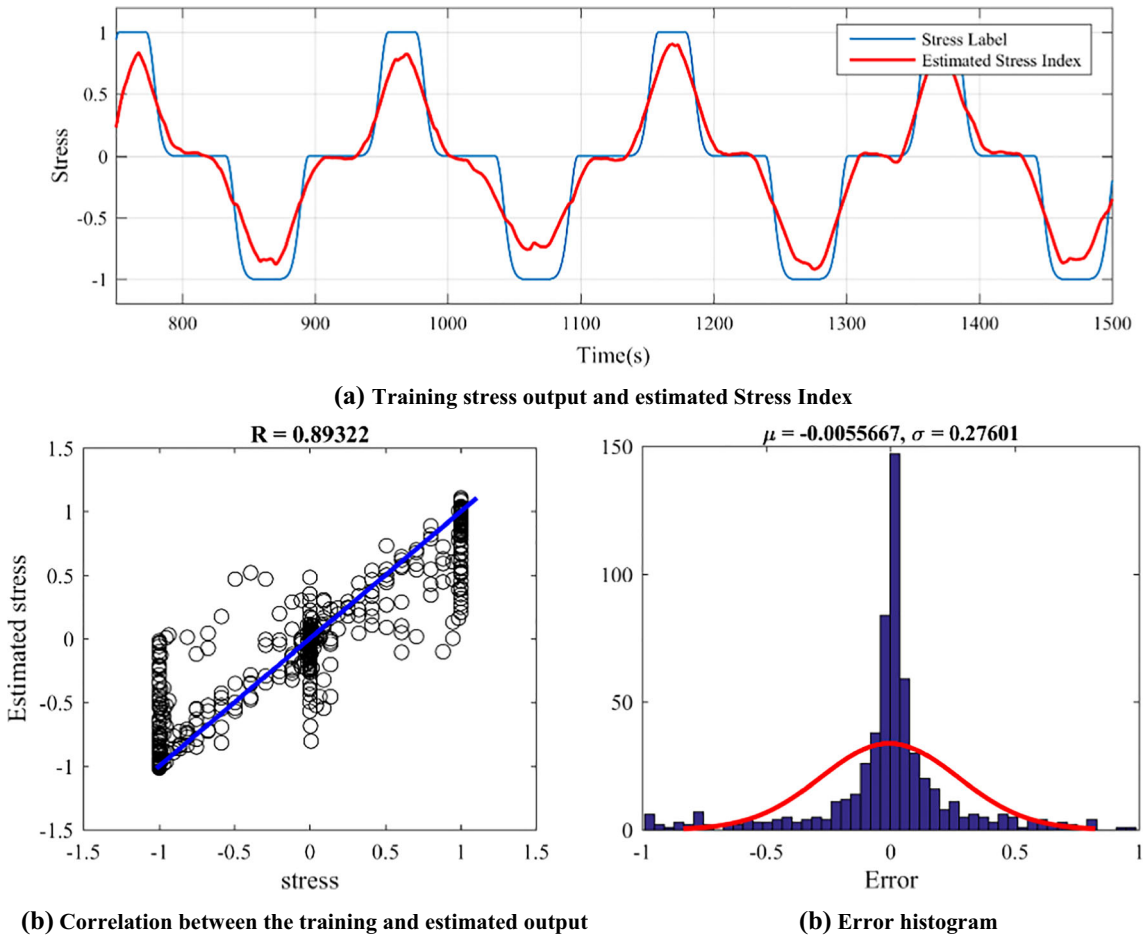


**(a) Training stress output and estimated Stress Index**

**(b) Correlation between the training and estimated output**

**(b) Error histogram**

**Fig. 21** Results of the estimation using SVR

## 6 Limitations and future works

Although in this research, we have tried to address the challenges of the continuous stress detection and develop a practical real-time stress monitoring system, there are still some points that might be interesting for further studies. Generally, one of the limitations of the physiological modeling studies is the issue of generalization of the obtained results. It means that in such studies, there are some factors that may affect the achieved results such as sensor types, testing conditions, health background of subjects, and dataset attributes. In this situation, choosing a large dataset can help to resolve the issue. In this study, we used a large dataset consisting of 63 sessions of 37 healthy subjects, aged between 24 and 27 years old, to make sure that the obtained results would be reliable and valid. Additionally, we replicated the modeling steps including signal normalization, signal selection, feature selection, classification, and SI estimation for several times. However, we may not draw a firm generalization from our results and we recommend other researchers to apply the proposed labeling and windowing method on other datasets with different age ranges and different sensor types. In addition, it might be interesting to calculate the

**Table 14** Estimation results

| Method | CC | Average error ($\mu$) | Error standard deviation ($\sigma$) |
|---|---|---|---|
| MLP ANN | 0.8623 | 0.068 | 0.3540 |
| RBF ANN | 0.7427 | − 0.051 | 0.4195 |
| ANFIS | 0.9281 | 0.008 | 0.2325 |
| SVR | 0.8864 | − 0.006 | 0.2870 |


**Fig. 22** The stress monitoring system

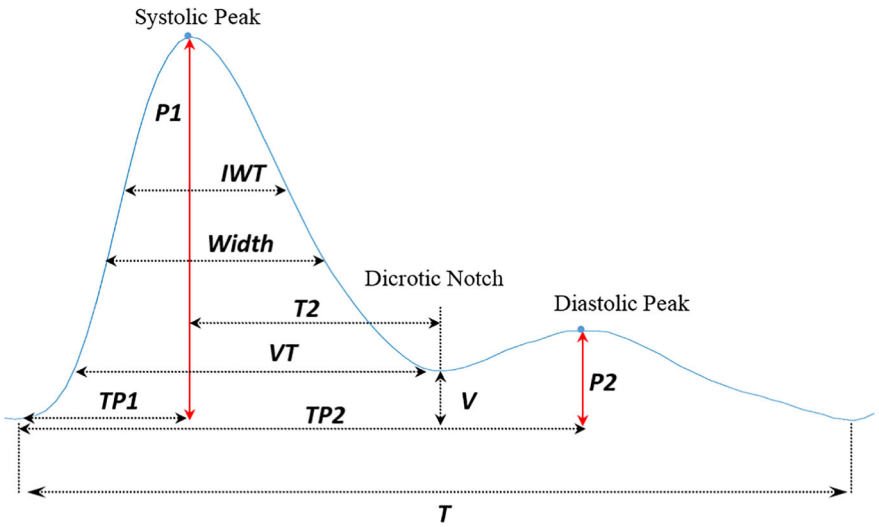


**(a) Characteristic parameters of a PPG pulse**

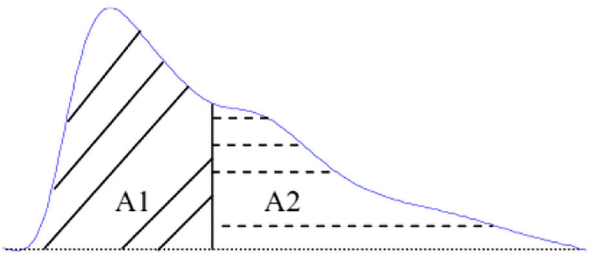


**(b) Areas under the PPG pulse wave separated at the dicrotic notch point** [58]

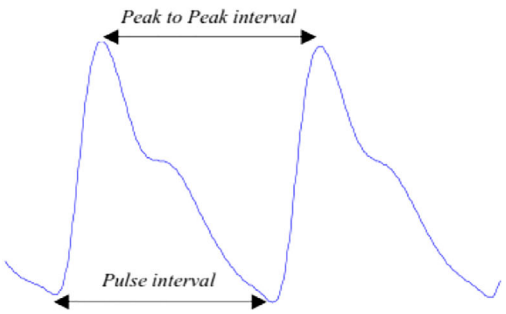


**(c) Two consecutive PPG waves** [58]

**Fig. 23** Characteristic parameters of PPG waveform

computational complexity of the proposed approach to estimate the time and amount of resources required for running the algorithm on an embedded system.

## Compliance with ethical standards

**Conflict of interest** The authors declare that they have no conflict of interests.

## Appendix

In this section, we will introduce all the extracted features from the PPG and GSR signals, used in this study. As mentioned in Sect. 3.1, 14 time and frequency domain features from GSR were extracted. As well as this, 38 features from PPG, 33 features from the derived HRV [46] and five features from the derived Cardiotach signals [45] were extracted. It is necessary to note that although some of the features are correlated with each other, using four feature selection methods could ensure us that the unusable features were eliminated before they were utilized in the modelings.

### PPG signal features

In Fig. 23, a typical PPG waveform and its characteristics are shown. Before introducing the extracted features, first we will name these characteristics:

- $P1$: Systolic amplitude [57]
- $P2$: Diastolic amplitude [57]
- $TP1$: Crest time (width of the wave from the beginning of the pulse to the systolic peak) [57]
- $TP2$: Dicrotic wave time (width of the wave from the beginning of the pulse to the diastolic peak) [57]
- IWT: Interwave time (width of the PPG pulse in two-thirds of the systolic peak) [57]
- Relative crest time $\left(\mathrm{RCT} = \frac{TP1}{TP2}\right)$ [57]
- Interwave distance $\left(\mathrm{IWD} = \frac{\mathrm{IWT}}{T}\right)$ [57]
- Relative dicrotic wave amplitude $\left(\mathrm{DWA} = \frac{P2}{P1}\right)$ [57]
- Relative dicrotic wave time $\left(\mathrm{DWT} = \frac{TP2}{T}\right)$ [57]
- $V$: Valley [59]
- Valley height ratio $\left(\mathrm{VHR} : \frac{V}{P1}\right)$ [59]
- $T2$ to $T$ ratio: $\left(T\mathrm{Ratio} = \frac{T2}{T}\right)$ [59]
- $A1$: Area under the first part of the PPG waveform separated at the dicrotic notch point [58]
- $A2$: Area under the second part of the PPG waveform separated at the dicrotic notch point [58]
- Width: The pulse width at the half height of the systolic peak [58]
- Inflection point area ratio $\left(\mathrm{IPA} = \frac{A2}{A1}\right)$ [58]
- $P2P_{\mathrm{bottom}}$, $T$: Pulse interval, Total Pulse duration [58]
- $P2P_{\mathrm{top}}$: Peak to Peak interval [58]

### PPG time domain features

| | | | |
|---|---|---|---|
| 1. | Mean of the normalized PPG | 21. | Mean of RCTs |
| 2. | Variance (VAR) of the normalized PPG | 22. | STD of RCTs |
| 3. | Mean of $P1$s | 23. | Mean of IWDs |
| 4. | Standard Deviation (STD) of $P1$s | 24. | STD of IWDs |
| 5. | Mean of $P2$s | 25. | Mean of VHRs |
| 6. | STD of $P2$s | 26. | STD of VHRs |
| 7. | Mean of $V$s | 27. | Mean of $T$Ratio s |
| 8. | STD of $V$s | 28. | STD of $T$Ratio s |
| 9. | Mean of Widths | 29. | Length of the PPG signal |
| 10. | STD of Widths | 30. | PPG Bandwidth [55] $\left(W = \frac{1}{2\pi}\sqrt{\frac{\sum_{i=2}^{N}(\mathrm{PPG}_i - \mathrm{PPG}_{i-1})^2}{\sum_{i=1}^{N}\mathrm{PPG}_i}}\right)$ |
| 11. | Mean $TP1$s | 31. | PPG fall time [55] (average of time of trough—time of preceding peak) in a segment |
| 12. | STD $TP1$s | 32. | Mean of $A1$s |
| 13. | Mean $TP2$s | 33. | Mean of $A2$s |
| 14. | STD $TP2$s | 34. | Mean of $A1 + A2$ |
| 15. | Mean of DWTs | 35. | Mean of IPAs |
| 16. | STD of DWTs | 36. | STD of IPAs |
| 17. | Mean of DWAs | | |
| 18. | STD of DWAs | | |
| 19. | Mean of IWTs | | |
| 20. | STD of IWTs | | |

### PPG signal frequency domain features

37. Power of the PPG signal in the Low-Frequency (LF) band (between 0.05 and 0.15 Hz) [60]
38. Power of the PPG signal in High-Frequency (HF) band (between 0.15 and 0.45 Hz) [60]

### Cardio tachometer (CardioTach) signal [45] features

39. 65th percentile of Cardiotach signal [45]
40. 70th percentile of Cardiotach signal [45]
41. 75th percentile of Cardiotach signal [45]
42. 85th percentile of derivative of Cardiotach signal [45]
43. 90th percentile of derivative of Cardiotach signal [45]

## HRV signal [45] features

### Time domain features

44. Mean of Heart Rates $\left(\text{HR}: \frac{60}{P2P_{\text{top}}}\right)$ [56]
45. STD of HRs [61]
46. Variance (VAR) of HRs
47. AVNN: Mean of $P2P_{\text{top}}$s [55]
48. SDNN: STD of $P2P_{\text{top}}$s [55]
49. VAR of $P2P_{\text{top}}$s
50. $\text{RMSSD}_{\text{top}}: \sqrt{\frac{1}{N}\left(\Delta D_i^2 + \Delta D_{i+1}^2 + \Delta D_{i+2}^2 + \cdots + \Delta D_{i+N}^2\right)}$, $\Delta D_i = P2P_{\text{top}_i} - P2P_{\text{top}_{i-1}}$ [55]
51. SDSD: STD of $\Delta D_i$s
52. EBC : $\max\left(P2P_{\text{top}}\right) - \min\left(P2P_{\text{top}}\right)$
53. NN50 [62]
54. PNN50 [56]
55. NN20 [55]
56. PNN20 [55]
57. Mean of $P2P_{\text{min}}$s
58. STD of $P2P_{\text{min}}$s
59. VAR of $P2P_{\text{min}}$s
60. $\text{RMSSD}_{\text{bottom}}: \sqrt{\frac{1}{N}\left(\Delta D_i'^2 + \Delta D_{i+1}'^2 + \Delta D_{i+2}'^2 + \cdots + \Delta D_{i+N}'^2\right)}$, $\Delta D_i' = P2P_{\text{bottom}_i} - P2P_{\text{bottom}_{i-1}}$
61. $\text{SDSD}_{\text{bottom}}$: STD of $\Delta D_i'$s
62. STD of HRV
63. STD of diff (HRV)

### Frequency domain features

64. Total of HRV signal between 0 and 0.4 Hz
65. Power of HRV signal in the Very-Low-Frequency (VLF) band (between 0 and 0.04 Hz) [56]
66. Power of HRV signal in the Low-Frequency (LF) band (between 0.04 and 0.15 Hz) [56]
67. Power of HRV signal in the Medium-Frequency (MF) band (between 0.08 and 0.15 Hz) [22]
68. Power of HRV signal in the High-Frequency (HF) band (between 0.15 and 0.4 Hz) [56]
69. LF/HF ratio [56]
70. Normalized LF (nLf) [56]
71. Normalized HF (nHF) [56]
72. Respiratory Sinus Arrhythmia (RSA) [63]

### Nonlinear HRV signal features

73. Short-term fluctuation slope in Detrended Fluctuation Analysis (DFA) [64]

**Poincaré plot indexes:**

74. $\text{SD}_1 = \sqrt{\frac{1}{2}\text{SDSD}^2}$ [62]
75. $\text{SD}_2 = \sqrt{2 \times \text{SDNN}^2 - \frac{1}{2}\text{SDSD}^2}$ [62]
76. $\text{SD}_1/\text{SD}_2$ ratio [62]

### GSR signal features

77. Mean of GSR signal [55]
78. VAR of GSR signal [55]
79. GSR peak rise time sum (Peak rise time) [55]
80. GSR peak amplitude sum (Peak amplitude) [55]
81. GSR peak energy sum (Peak energy): $\sum \frac{1}{2}\text{Amplitude} \times \text{Risetime}$ [55]
82. The amplitude of the highest Skin Conductance Responses (SCRs)
83. The rise time of the highest SCR
84. Number of GSR peaks [55]
85. Mean power of the GSR signal
86. $\text{GSR}_{\text{Bwidth}} = \frac{1}{2\pi}\sqrt{\frac{\sum D_{\text{GSR}_i}^2}{\sum \text{GSR}_i^2}}$, $D_{\text{GSR}_i} = \text{GSR}_i - \text{GSR}_{i-1}$
87. Mean of rising rate: sum average of the first derivative of points with the first derivative > threshold (0.4) [55]
88. Mean of decay rate: sum average of the first derivative of points with the first derivative < threshold (− 0.4) [55]
89. GSR percentage decay: percentage of time samples in a given segment with the first derivative < 0 [55]
90. Difference between 65th percentile of the GSR signal and 15th percentile of the GSR signal [45]

## References


1. Cacioppo J, Tassinary LG, Berntson GG (2007) The handbook of psychophysiology, vol 44. Cambridge University Press, Cambridge
2. Cannon WB (1929) Bodily changes in pain, hunger, fear and rage. D. Appleton Co, New York, pp 360–376
3. McCorry LK (2007) Physiology of the autonomic nervous system. Am J Pharm Educ 71(4):78
4. Wei CZ (2013) Stress emotion recognition based on RSP and EMG signals. Adv Mater Res 709:827–831
5. Kaklauskas A et al (2011) Web-based biometric computer mouse advisory system to analyze a user's emotions and work productivity. Eng Appl Artif Intell 24(6):928–945
6. Asai K (2008) The role of head-up display in computer-assisted instruction. In: Asai K (ed) Human computer interaction: new developments. InTech. ISBN: 978-953-7619-14-5. https://www.intechopen.com/books/human_computer_interaction_new_developments/the_role_of_headup_display_in_computer-assisted_instruction

7. Lu H et al (2012) Stresssense: detecting stress in unconstrained acoustic environments using smartphones. In: Proceedings of the 2012 ACM conference on ubiquitous computing, Pittsburgh, Pennsylvania, Sept. 05–08, pp 351–360
8. Hagmüller M, Rank E, Kubin G (2006) Evaluation of the human voice for indications of workload-induced stress in the aviation environment. EEC Note, vol 18, no. 06
9. Patil VP, Nayak KK, Saxena M (2013) Voice stress detection. Int J Electr Electron Comput Eng 2(2):148–154
10. Zhang H, Zhu Y, Maniyeri J, Guan C (2014) Detection of variations in cognitive workload using multi-modality physiological sensors and a large margin unbiased regression machine. In: 2014 36th Annual international conference of the IEEE engineering in medicine and biology society (EMBC), Chicago, Illinois, Aug. 26–30, pp 2985–2988
11. Ramos J, Hong J-H, Dey AK (2014) Stress recognition—a step outside the Lab. In: PhyCS, pp 107–118
12. Madokoro H, Sato K (2012) Facial expression spacial charts for describing dynamic diversity of facial expressions. J Multimed 7(4):314–324
13. Jabon M, Bailenson J, Pontikakis E, Takayama L, Nass C (2011) Facial expression analysis for predicting unsafe driving behavior. IEEE Pervasive Comput 10(4):84–95
14. Liao W, Zhang W, Zhu Z, Ji Q (2005) A real-time human stress monitoring system using dynamic bayesian network. In: 2005 IEEE computer society conference on computer vision and pattern recognition (CVPR'05)—workshops. San Diego, CA, USA, Sept. 21–23, p 70
15. Kapoor A, Picard RW (2005) Multimodal affect recognition in learning environments. In: Proceedings of the 13th annual ACM international conference on Multimedia, Hilton, Singapore, Nov. 06–11, pp. 677–682
16. Alberdi A, Aztiria A, Basarab A (2016) Towards an automatic early stress recognition system for office environments based on multimodal measurements: a review. J Biomed Inform 59:49–75
17. Cinaz B, Arnrich B, La Marca R, Tröster G (2013) Monitoring of mental workload levels during an everyday life office-work scenario. Pers Ubiquitous Comput 17(2):229–239
18. Wijsman J, Grundlehner B, Penders J, Hermens H (2010) Trapezius muscle EMG as predictor of mental stress. In: Wireless Health 2010, San Diego, California, Oct. 05–07, pp 155–163
19. Hjortskov N, Rissén D, Blangsted AK, Fallentin N, Lundberg U, Søgaard K (2004) The effect of mental stress on heart rate variability and blood pressure during computer work. Eur J Appl Physiol 92(1–2):84–89
20. Rahnuma KS, Wahab A, Kamaruddin N, Majid H (2011) EEG analysis for understanding stress based on affective model basis function. In: 2011 IEEE 15th International symposium on consumer electronics (ISCE), Singapore, Singapore, June 14–17, pp 592–597
21. Seo S-H, Lee J-T (2010) Stress and EEG. In: Crisan M (ed) Convergence and hybrid information technologies. InTech, pp 413–426
22. Healey JA, Picard RW (2005) Detecting stress during real-world driving tasks using physiological sensors. IEEE Trans Intell Transp Syst 6(2):156–166
23. Wijsman J, Grundlehner B, Liu H, Penders J, Hermens H (2013) Wearable physiological sensors reflect mental stress state in office-like situations. In: *2013* Humaine association conference on affective computing and intelligent interaction (ACII), Geneva, Switzerland, Sept. 02–05, pp 600–605
24. Shi Y et al (2010) Personalized stress detection from physiological measurements. In: International symposium on quality of life technology, Las Vegas, USA, June 28–29, pp 28–29
25. Zhai J, Barreto A (2006) Stress detection in computer users based on digital signal processing of noninvasive physiological variables. In: 28th Annual international conference of the IEEE engineering in medicine and biology society, 2006. EMBS'06, New York, 30 Aug.–3 Sept., pp 1355–1358
26. McDuff D, Karlson A, Kapoor A, Roseway A, Czerwinski M (2012) AffectAura: an intelligent system for emotional memory. In: Proceedings of the SIGCHI conference on human factors in computing systems, Austin, TX, USA, May 05–10, pp 849–858
27. Kocielnik R, Sidorova N, Maggi FM, Ouwerkerk M, Westerink JHDM (2013) Smart technologies for long-term stress monitoring at work. In: 2013 IEEE 26th International symposium on computer-based medical systems (CBMS), Porto, Portugal, June 20–22, pp 53–58
28. Kurniawan H, Maslov AV, Pechenizkiy M (2013) Stress detection from speech and galvanic skin response signals. In: Proceedings of the 26th IEEE international symposium on computer-based medical systems, Porto, Portugal, June 20–22, pp 209–214
29. Chigira H, Kobayashi M, Maeda A (2012) Mouse with photoplethysmographic surfaces for unobtrusive stress monitoring. In: 2012 IEEE International conference on consumer electronics-Berlin (ICCE-Berlin), Berlin, Germany, Sept. 3–5, pp 304–305
30. Garbarino M, Lai M, Bender D, Picard RW, Tognetti S (2014) Empatica E3—a wearable wireless multi-sensor device for real-time computerized biofeedback and data acquisition. In: 2014 EAI 4th International conference on wireless mobile communication and healthcare (Mobihealth), Athens, Greece, Nov. 3–5, pp 39–42
31. Burns A et al (2010) SHIMMER$^{TM}$—a wireless sensor platform for noninvasive biomedical research. IEEE Sens J 10(9):1527–1534
32. Peper E, Harvey R, Lin I-M, Tylova H, Moss D (2007) Is there more to blood volume pulse than heart rate variability, respiratory sinus arrhythmia, and cardiorespiratory synchrony? Biofeedback 35(2):54–61
33. Lu G, Yang F, Taylor JA, Stein JF (2009) A comparison of photoplethysmography and ECG recording to analyse heart rate variability in healthy subjects. J Med Eng Technol 33:634–641
34. Boucsein W (2012) Electrodermal activity. Springer, Berlin
35. Norton T, Piette D, Exadaktylos V, Berckmans D (2018) Automated real-time stress monitoring of police horses using wearable technology. Appl Anim Behav Sci 198:67–74
36. Pandey P, Lee EK, Pompili D (2016) A distributed computing framework for real-time detection of stress and of its propagation in a team. IEEE J Biomed Health Inform 20:1502–1512
37. Minguillon J, Perez E, Lopez-Gordo MA, Pelayo F, Sanchez-Carrion MJ (2018) Portable system for real-time detection of stress level. Sensors (Switzerland) 18:2504
38. Bin MS, Khalifa OO, Saeed RA (2016) Real-time personalized stress detection from physiological signals. In: Proceedings—2015 International conference on computing, control, networking, electronics and embedded systems engineering, ICCNEEE 2015
39. Research Center for Development of Advanced Technologies. http://en.rcdat.ir. Accessed 15 Sept 2018
40. Tarvirdizadeh B, Golgouneh A, Khodabakhshi E, Tajdari F (2017) An assessment of a similarity between the right and left hand photoplethysmography signals, using time and frequency features of heart-rate-variability signal. In: IEEE 4th International conference on knowledge-based engineering and innovation (KBEI), Tehran, Iran, Dec. 22
41. Tarvirdizadeh B, Golgouneh A, Tajdari F, Khodabakhshi E (2018) A novel online method for identifying motion artifact and photoplethysmography signal reconstruction using artificial neural networks and adaptive neuro-fuzzy inference system. Neural Comput Appl. https://doi.org/10.1007/s00521-018-3767-8
42. De Santos A, Sánchez-Avila C, Bailador-Del Pozo G, Guerra-Casanova J (2011) Real-time stress detection by means of physiological signals. INTECH Open Access Publisher, Rijeka

43. Slavkovic A (2002) Evaluating polygraph data. Technical Report 766. Department of Statistics, Carnegie Mellon University, pp 1–27
44. Craig RA, Raskin DC, Kircher JC (2011) The use of physiological measures to detect deception in juveniles. Polygraph 40(2):86
45. Harris JC, McQuarrie AD (2009) The preliminary credibility assessment system embedded algorithm description and validation results. Johns Hopkins University Applied Physics Laboratory Report Number GED
46. Stauss HM (2003) Heart rate variability. Am J Physiol Integr Comp Physiol 285(5):R927–R931
47. Peng H, Long F, Ding C (2005) Feature selection based on mutual information criteria of max-dependency, max-relevance, and min-redundancy. IEEE Trans Pattern Anal Mach Intell 27(8):1226–1238
48. Wu X, Yu K, Ding W, Wang H, Zhu X (2013) Online feature selection with streaming features. IEEE Trans Pattern Anal Mach Intell 35(5):1178–1192
49. Lancaster HO, Seneta E (2005) Chi Square distribution. Wiley Online Library, New York
50. Zhou J, Foster D, Stine R, Ungar L (2005) Streaming feature selection using alpha-investing. In: Proceedings of the eleventh ACM SIGKDD international conference on knowledge discovery in data mining, Chicago, Illinois, USA, Aug. 21–24, pp. 384–393
51. Zare H, Niazi M (2016) Relevant based structure learning for feature selection. Eng Appl Artif Intell 55:93–102
52. Broomhead DS, Lowe D (1988) Radial basis functions, multivariable functional interpolation and adaptive networks. Royal Signals and Radar Establishment Malvern (United Kingdom)
53. Haykin S, Network N (2004) A comprehensive foundation. Neural Netw 2(2004):41
54. Jang J-S (1993) ANFIS: adaptive-network-based fuzzy inference system. IEEE Trans Syst Man Cybern 23(3):665–685
55. Singh RR, Conjeti S, Banerjee R (2013) A comparative evaluation of neural network classifiers for stress level analysis of automotive drivers using physiological signals. Biomed Signal Process Control 8(6):740–754
56. Salahuddin L, Cho J, Jeong MG, Kim D (2007) Ultra short term analysis of heart rate variability for monitoring mental stress in mobile settings. In: 29th Annual international conference of the IEEE engineering in medicine and biology society, 2007. EMBS 2007. Lyon, France, Aug. 22–26, 2007, pp 4656–4659
57. Korpas D, Halek J, Dolezal L (2009) Parameters describing the pulse wave. Physiol Res 58(4):473
58. Elgendi M (2012) On the analysis of fingertip photoplethysmogram signals. Curr Cardiol Rev 8(1):14–25
59. Hlimonenko I, Meigas K, Vahisalu R (2003) Waveform analysis of peripheral pulse wave detected in the fingertip with photoplethysmograph. Measur Sci Rev 3(2):49–52
60. Yoshizawa M et al (2004) Assessment of emotional reaction induced by visual stimulation based on cross-correlation between pulse wave transmission time and heart rate in the Mayer wave-band. In: 26th Annual international conference of the IEEE engineering in medicine and biology society, 2004. IEMBS'04, San Francisco, CA, USA, Sept. 1–5, vol 1, pp 2411–2414
61. Sun F-T, Kuo C, Cheng H-T, Buthpitiya S, Collins P, Griss M (2010) Activity-aware mental stress detection using physiological sensors. In: International conference on mobile computing, applications, and services, Santa Clara, CA, USA, Oct. 25–28, pp 211–230
62. Muaremi A, Arnrich B, Tröster G (2013) Towards measuring stress with smartphones and wearable devices during workday and sleep. Bionanoscience 3(2):172–183
63. McSharry PE, Clifford GD, Tarassenko L, Smith LA (2003) A dynamical model for generating synthetic electrocardiogram signals. IEEE Trans Biomed Eng 50(3):289–294
64. Dimitriev DA, Saperova EV, Dimitriev AD (2016) State anxiety and nonlinear dynamics of heart rate variability in students. PLoS ONE 11(1):e0146131